

INSTRUMENTATION

## Simulated ECT of the Left Ventricle Using Rotating Slant-Hole Collimator and Two Camera Positions

Kenneth F. Koral, Craig Nolder, Glen Ciliax, W. Leslie Rogers, and John W. Keyes, Jr

*University of Michigan Medical Center, Ann Arbor, Michigan*

**Limited-angular-range tomography leads to an elongating distortion of the object in the direction of the z axis (perpendicular to the camera face). Two-view tomography appends to the usual data set another set of projections taken after the camera is rotated 90° about an axis perpendicular to z. We investigated two-view tomography using a rotating-slant-hole collimator, 12 projections per view and the SMART iterative algorithm. Computer simulations extended previous results to include noise and attenuation. Phantoms imaged were the Au-rings in air and a ventricle phantom angled with respect to the z axis and placed in a water bath. Two-view results were generally superior compared to one-view results, were subject to some artifact in imaging defects, but could detect defects by looking at the differences between two sets of images, and were fairly insensitive to ventricle angulation. Therefore, two-view tomography has promise for thallium-type imaging.**

**J Nucl Med 25: 343–351, 1984**

Emission computerized tomography (ECT) with limited-angular-range collimators such as the seven-pinhole (1), pinhole time-coded aperture (2), rotating slant-hole (3), and quadrant slant-hole (4) samples a three-dimensional volume over a solid angle less than the  $2\pi$  needed for complete sampling. It is now well known that the results are an elongating distortion of the object in the direction perpendicular to the camera face. Further data processing seems able to correct the problem only in cases where the sampling is almost complete (5,6).

We have asked the question: Is it possible to sharpen the depth resolution by taking a second set of projections with the same type of collimator but with the camera swung through 90° to an orthogonal viewing position? The envisioned geometry is shown in Fig. 1, which assumes a rotating slant-hole collimator. A similar investigation using the seven-pinhole collimator is now in progress (7). Our initial computer-simulated results (8)

lead to cautious optimism. We examine the question further in this paper with computer simulations that take into account attenuation and noise, and with phantom simulations that approximate thallium heart imaging.

Potential advantages of the above approach to tomographic heart imaging are: (a) the requirement of only a basically standard camera; (b) the possibility of bedside imaging in the intensive-care unit; (c) relative to transverse-section tomography, the need for accurate camera calibration in only two, rather than many, orientations, and closer proximity of the camera to the object during the entire time of data acquisition than is the case with 360° rotation; and (d) compared with seven-pinhole tomography, the elimination of the need to position the camera looking down the long axis of the left ventricle. A disadvantage is the need to develop a simple and accurate means to obtain the orthogonal camera position while maintaining a known geometric relation between the camera and the heart.

Received July 13, 1983; revision accepted Oct. 24, 1983.

For reprints contact: Kenneth F. Koral, PhD, Div. of Nucl. Med., Box 021, University of Michigan Med. Ctr., 1405 E. Ann St., Ann Arbor, MI 48109.

### MATERIALS AND METHODS

**Imaging system.** For both the simulated and phantom data presented in this paper, 12 separate images form the

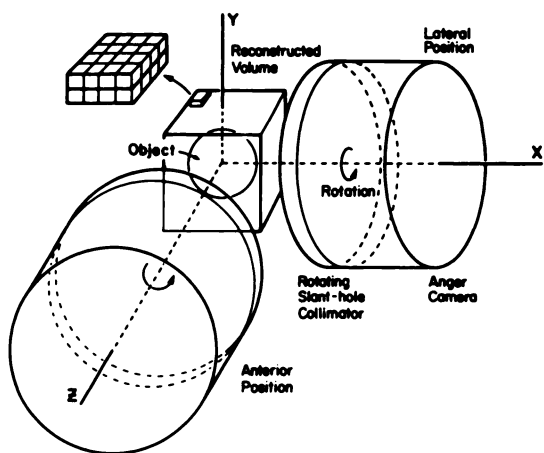


**FIG. 1.** Envisioned clinical geometry for two-view tomography. Camera is first positioned as close as possible to and over left ventricle in anterior position. Rotating slant-hole collimator is successively rotated about z axis to record 12 separate projections. Then camera is swung 90° about y axis to lateral position, being shifted back to clear body. Here, 12 more projections are recorded as collimator rotates about x axis. Cubical volume centered about ventricle is then reconstructed from 24 projections.

anterior projection set and the same number form the lateral set. In between each projection image, the slant-hole collimator is rotated 30° about its axis of rotation. Figure 2 shows a representative group of four images from the anterior view and four representative images from the lateral view for experimental data taken with the Au-rings phantom. The symmetry axis of the phantom is aligned parallel with the axis of the collimator rotation in the anterior view, as shown in Fig. 3.

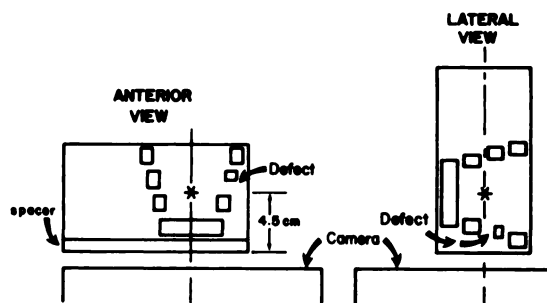


**FIG. 3.** Commercial Au-rings phantom with one end of plastic blocks removed. Phantom itself could then be rotated to simulate two viewing positions. Its "center," marked by \*, is at same distance from camera in both views.

In the lateral view of Fig. 2, the one quadrant defect located in the third ring can be seen in the 180° image, and the 5.1-mm gaps between active regions of emitter are visible in the 90° and 270° images.

**Simulations.** Images are formed by forward-projecting a digitized version of the object. Uniform intensity in the object is assumed except for half-strength or zero-strength defects. Size of a detector element is a 3.4 mm square, which leads to a 3.4-mm cubic image element (see Fig. 1). The collimator's slant angle is a parameter taking on values of 26° and 45°. Fall-off of a parallel-hole collimator's resolution with distance is not simulated. Likewise, no attempt is made to simulate Compton scattering or background from blood and organs other than the left ventricle. Noise is added to the individual views as Gaussian-distribution noise with a standard deviation equal to 10% of the counts in the pixel. At-

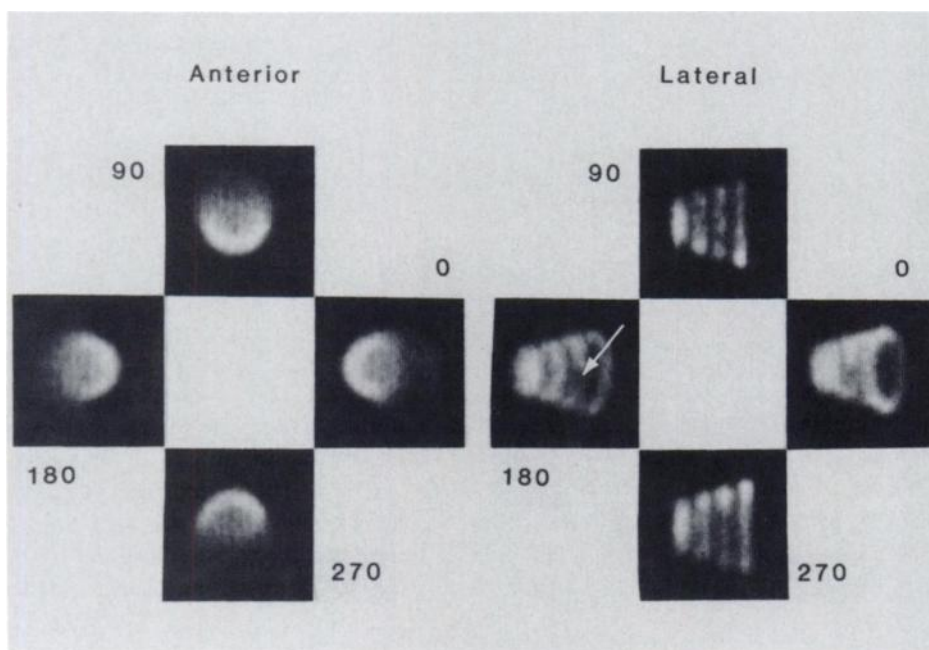


**FIG. 2.** Representative four projection images from anterior view and same number from lateral view, for experimental data taken with Au-rings phantom. Angles listed are those of collimator rotation. White arrow points to one-quadrant defect as imaged in 180° lateral projection. Note nonuniformity due to plastic attenuation for 90° and 270° lateral projections.

**TABLE 1. DIAMETERS FOR ACTIVE RINGS OF STACKABLE GOLD-RINGS PHANTOM**

Ring No.	Inner diameter	Outer diameter
1	0 cm	5.0 cm
2	4.0 cm	6.0 cm
3A	5.0 cm	7.0 cm
4	6.0 cm	8.0 cm

tenuation is assumed to be uniform, with an absorption coefficient of  $0.19 \text{ cm}^{-1}$  to simulate attenuation of the radiation from Tl-201.

The objects investigated are a spherical shell, the Au-rings phantom, and a half-ellipsoid-of-revolution shell. Outer diameter of the sphere is 8.0 cm, with a 1.0 cm wall thickness. A one-quadrant half-strength defect, 1 cm thick, can be placed in the xy plane. The Au-rings phantom simulation has individual blocks 6 pixels thick (2.04 cm) containing an active ring or disk 4 pixels thick (1.36 cm). Diameters of individual rings are the same as for the phantom and are given in Table 1. The rings are stacked in the order 1 through 4 and are placed with Ring 1 toward the camera for the anterior view. When attenuation is included in the data simulation, a point on the axis of symmetry midway between Rings 2 and 3A is assumed to be 4.5 cm from the crystal in both views, and the entire volume in front of the camera is assumed to be uniformly attenuating. The half-ellipsoid-of-revolution shell is angled so that its long axis lies either  $20^\circ$  or  $40^\circ$  to the left of anterior and  $40^\circ$  inferior to a transverse section. The dimensions of the ellipsoid are given by the equation for the inside wall (before rotation):

$$\left(\frac{z}{7.3 \text{ cm}}\right)^2 + \left(\frac{x}{3.7 \text{ cm}}\right)^2 + \left(\frac{y}{1.8 \text{ cm}}\right)^2 = 1 \text{ for } x > 0,$$

and by the wall thickness of 1.3 cm (9). Data are generated both with and without a defect 1 cm thick being placed in the xy plane (before rotation) half-way between the "apex" and the "base" of the ventricle. It covers one quadrant in angular extent.

**Phantoms.** Phantoms are measured with a portable camera having a small field of view and carrying a rotating collimator having a  $25^\circ$  slant angle. The voxel size consistent with  $128 \times 128$  acquisition is now 2.2 mm. The lateral view is obtained by rotating the phantom an accurate  $90^\circ$  with the camera fixed, rather than by swinging the camera about an immobile target, as would be the case in the clinical setting. This method of imaging the Au-195 rings is shown by the sketches of Fig. 3. A point-source calibration set of images is also taken with a point source at the center of the object, which is at a known distance from the camera face. For the Au rings, rotation of the phantom is about an axis that passes through this point. An average of 90,000 counts was

accumulated for each of the 24 2-min projections, giving a total of  $\sim 2.2$  million counts.

To simulate more closely the clinical situation, a continuous-shell left-ventricle phantom was constructed, so that its long axis points  $30^\circ$  left of anterior and  $23^\circ$  inferior to a transverse section (10). The phantom is rotationally symmetric about the long axis; outer length of the long axis is 9.5 cm, outer diameter of the largest circular cross section is 5.7 cm, and shell thickness is 1 cm. The shell is filled with a solution of Tc-99m. A 5-ml defect of Apiezon wax can be inserted to cover one quadrant in the plane of the largest cross section.

To simulate body attenuation, the left-ventricle phantom is placed in a water bath (Fig. 4). To match real anatomy more closely, the distance of the "center" of the ventricle from the bottom of the bath is increased from 7 cm for the anterior view to 12.7 cm for the lateral view. Calculated transmission to the center is 30.3% for the anterior view and 11.2% for the lateral view. To compensate for the greater distance, two sets of images with a point source at the phantom's "center" (shown as an asterisk) are required. Because of the lower count rate due to greater attenuation, each lateral projection is measured for three times as long as each anterior projection. Counts for all projections totaled 1.7 million, both for the case with the defect and the case without the defect.

**Algorithm.** For reconstruction the SMART algorithm (11) is used without "background" subtraction. The steps of the basic algorithm are detailed in Ref. 8. Two methods of correcting for uniform attenuation are tested. In the first, the data are reconstructed ignoring attenuation, then the resulting images are multiplied by a compensation matrix (12). For a given pixel  $j$ , the transmission to the body surface,  $T_{ij}$ , is averaged over the 24 projections to produce  $\bar{T}_j$ :

$$\bar{T}_j = \frac{1}{24} \sum_{i=1}^{24} T_{ij}$$

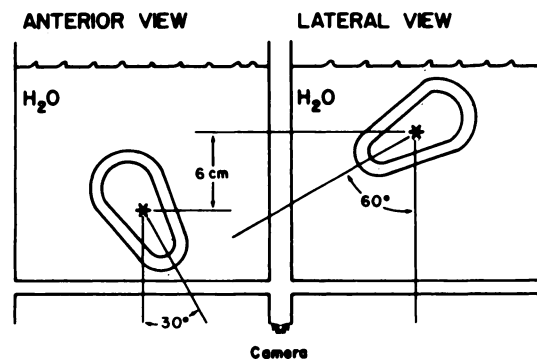


**FIG. 4.** Angled left-ventricle phantom placed in water bath. Phantom is again itself rotated about its "center," marked by \*, but in addition it is shifted 6 cm away from camera for lateral-view projections. Angulation of long axis is  $30^\circ$  left of lateral as shown and is also  $23^\circ$  inferior to transverse section, that is, into page.

The compensation factors,  $C_j$ , are formed from the inverse of the  $\bar{T}_j$

$$C_j = 1/\bar{T}_j$$

In the second method, the calculated transmissions are utilized in the iterative reconstruction itself. Moreover, they may or may not be introduced into the initial impedance estimate. Within the algorithm, the  $i$ th ray sum in the  $\rho$ th iteration,  $R_i^{\rho-1}$ , is computed using the transmissions  $T_{ij}$ , as weights

$$R_i^{\rho-1} = \sum_j T_{ij} I_j^{\rho-1}$$

where  $I_j^{\rho-1}$  is the  $j$ th image element. The  $i$ th element of the error projection,  $E_i^{\rho-1}$ , is calculated as before:

$$E_i^{\rho-1} = P_i - R_i^{\rho-1},$$

where  $P_i$  is the  $i$ th projection element. Instead of averaging over the  $E_i^{\rho-1}$  to update the  $j$ th image element, as previously, one now averages over the  $E_i^{\rho-1}$  weighted by a function of  $T_{ij}$ . The functions we have investigated are  $T_{ij}$ , 1,  $1/\sqrt{T_{ij}}$  and  $1/T_{ij}$ .

In the impedance first estimate, one replaces the inverses of the projection with weighted inverses:

$$\frac{1}{I^0} = \frac{T_1}{P_1} + \frac{T_2}{P_2} + \dots + \frac{T_{24}}{P_{24}}$$

Here  $I^0$  is the image's initial estimate and the subscripts for pixel number have been suppressed.

**Data analysis.** A total-volume accuracy measure,  $A$ , is computed for the results of the computer simulations by

$$A = \frac{\frac{1}{M} \sum |I_i - O_i|}{\frac{1}{M} \sum O_i},$$

where  $M$  is the total number of elements in the volume,  $I_i$  is the  $i$ th voxel of the final image, and  $O_i$  is the  $i$ th voxel of the object. A similar accuracy measure for only a slice containing a given number of planes is similarly defined. A small value of  $A$  indicates good agreement between the strengths of the reconstructed image and the true object. In addition, circumferential plots are made for both simulation and phantom results. Images and plots for the angled ventricles are made after the results are rerotated through the known angles by a standard computer program (13). All circumferential plots are for slices that are a sum over three or four of the individual planes.

RESULTS

**Two views compared with one view. Spherical shell simulation.** Two-view results from the noiseless, attenuation-free, uniform-strength spherical shell have slight deviations from uniformity similar to those plotted in

Ref. 8. These nonuniformities are not completely eliminated by increasing the collimator's slant angle to 45°.

Nevertheless, with the 26° slant angle and the centrally located, one-quadrant defect, the two views produce an accuracy measure that is 4.2 times better for the entire volume and 3.3 times better for the defect slice than the results with one view (see Table 2).

**Au-rings phantom.** Figure 5 shows a comparison of the two-view results to the one-view reconstruction from only the anterior 12 projections. It is seen that the two-view results are much more faithful to the original object. The defect in Ring 3A is clearly seen in the slice at 4.2 cm. The 5-mm photopenic gaps between rings are observed in the slice at 2.5 cm, which was close to the camera in the lateral view, but not in the slice at 9.5 cm, which was farther away. In this case the phantom was perfectly aligned for the one-view data acquisition. Although it is not readily apparent from the figure, the defect in Ring 3A can be detected at the correct location in the one-view images with a circumferential plot. Likewise not apparent is that Ring 4 in the two-view images shows up a nonuniformity artifact in the circumferential plots for planes slicing the  $z$  axis, due at least partly to the unavoidable attenuation of the plastic.

**Two views for cases approaching the clinical situation.**

**Au-rings simulations.** The results of the reconstructions from the noiseless simulated data for the Au-rings object are shown in Table 3. We find that the addition of attenuation to the simulation worsens the magnitude of the nonuniformity in Ring 4 to the point where it must be called an artifact. As a function of the type of data and of the reconstruction parameters, the table lists the accuracy measures for the total volume, for the defect slice, and for the Ring 4 slice, as well as the contrast of the defect compared with the contrast of the artifact. Here circumferential-plot contrast is defined as the strength at the given angle divided by the maximum strength.

It is seen that attenuated data, compared with perfect nonattenuated data (Run 80 compared with 79), worsen all accuracy measures and introduce an artifactual contrast at 180° equal to 40%. Attempts at attenuation correction did not succeed in attaining the quality of the reconstruction with the perfect data in any case. The

**TABLE 2. ACCURACY MEASURE FOR COMPUTER-SIMULATED, NOISELESS, ATTENUATION-FREE SPHERICAL SHELL WITH HALF-STRENGTH DEFECT**

Number of views	Run No.	Accuracy measure, A	
		Total volume	Defect slice
2	46	0.21	0.14
1	47	0.89	0.47

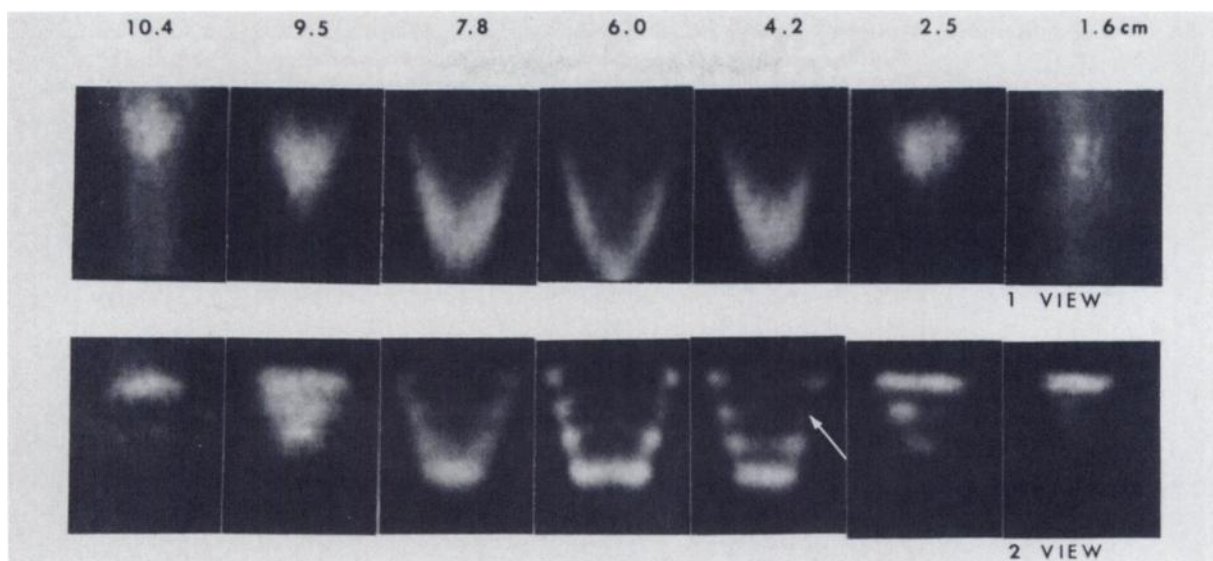


FIG. 5. Comparison of 2-view reconstruction with 1-view reconstruction for experimental data from Au-rings phantom. Imaging geometry is as shown in Fig. 3. Values listed are distances of slices from camera face in lateral position. Geometric distortion of 1-view reconstruction is clear. White arrow points to quadrant defect in Ring 3A.

total-accuracy measure, which measures absolute agreement, gradually worsens as the backprojection weights change from proportional to T to inversely proportional to T. Of perhaps more importance, the best contrast for the artifact is 72% instead of 100% with T, 1/T correction, but the defect contrast is 50% instead of 0%. Attenuation compensation produces a nearly perfect defect contrast of 2%, but the artifact contrast worsens to 48%.

*Individual half-ellipsoidal-shell simulations.* The results of the two-view reconstructions from the simulated data for a half-ellipsoidal shell are given in Table 4 and Fig. 6. The shell contains a defect and is angulated 40° lateral and 40° inferior. The first two entries of the

table (Run 74 compared with 75) show that the addition of 10% Gaussian noise has a rather small effect; the total-volume accuracy measure worsens only from 0.62 to 0.63 and the contrasts are very similar.

The circumferential plot for a slice located between apex and defect for Run 74 is shown in Fig. 6 and labeled “26° slant angle.” Here the data have been normalized so that the mean value is 100. The correct shape for this plane is then the straight line at this value. The dip seen from 170–360° is near the angular location of the true defect, 270–360°. The lack of uniformity is improved, as seen in the dashed line, by simulating a new data set taken with a 45° slant angle collimator (Run 91 of Table 4) The standard deviation of the circumferential plot

TABLE 3. ACCURACY OF RESULTS FOR SIMULATED AU-RINGS PHANTOM WITH DEFECT; COLLIMATOR SLANT ANGLE = 26°

Attenuated data?	Attenuation correction?	Initial estimate	Run No.	Accuracy measure, A			Artifact location	Contrast in %	
				Total	Defect	Ring 4		Defect	Artifact
No	No	Impedance	79	0.79	0.79	0.66	None	6	74
Yes	No	Impedance	80	0.97	0.97	0.96	180°	12	40
Yes	T, T†	Zero	90	1.17	1.06	1.02	180°	53	24
Yes	T, 1	Zero	85	1.38	1.16	1.22	180°	58	60
Yes	T, 1	Wt. imp.*	87	1.38	1.16	1.07	180°	66	60
Yes	T, 1/√T	Zero	92	1.67	1.31	1.13	0°, 180°	58	72
Yes	T, 1/T	Zero	86	2.43	1.62	1.26	0°	56	64
Yes	T, 1/T	Impedance	89	2.43	1.62	1.26	0°	50	72
Yes	T, 1/T	Wt. Imp.	88	2.38	1.62	1.25	0°	58	64
Yes	Compensation	Impedance	80/Comp	—	—	—	0°, 180°	2	48

\* Wt. imp = weighted impedance.

† Entry before comma indicates weighting used in forward projection, and that after comma weighting in back projection. T = transmission.

**TABLE 4. ACCURACY OF RESULTS FOR SIMULATED HALF-ELLIPSOIDAL SHELL WITH DEFECT; ANGULATION IS 40° LATERAL AND 40° INFERIOR**

Attenuated data?	Attenuation correction?	Slant angle	Noise added?	Run No.	Total accuracy measure, A	Artifact location	Contrast in % Defect	Artifact
No	No	26°	No	74	0.62	Apical plane 315°	18	68
No	No	26°	10%	75	0.63	Apical plane 315°	18	66
No	No	45°	No	91	0.61	Apical plane 315°	20	80
Yes	No	45°	No	91/R2	0.94	Basal plane 90°	22	44
Yes	T, $1/\sqrt{T}$	45°	No	96	1.57	Basal plane 180°	48	72
Yes	T, 1/T	45°	No	95	2.28	Basal plane 270°	38	56
Yes	Compensation	45°	10%	107	—	Basal plane 180°	16	64

drops from 11.9 to 5.9 with the increase in slant angle. The use of a 45° slant angle is, therefore, assumed for the remaining simulations of the paper (run numbers >90).

Table 4 shows that the inclusion of attenuation in the simulated data causes the accuracy of the reconstruction to decrease for the half-ellipsoidal shell, as it did for the Au rings. The accuracy measure worsens from 0.61 to 0.94 (Run 91 compared with 91/R2). Attempts at attenuation correction are again generally unsuccessful for this object; compensation and T,  $1/\sqrt{T}$  correction do a better job than T, 1/T correction.

*Differences between half-ellipsoidal-shell simulations.* Since attenuation correction is unable to produce an artifact-free result for either object tested, we turn our attention to the question of whether a defect can be detected by differencing two images (one with and one without a defect). The following comparisons of reconstructions are carried out for data with noise, attenua-

tion, and attenuation compensation. (We note that the addition of the 10% noise has very little effect.) The results are that the circumferential plots are quite similar in the slices without defects and are dissimilar only in the correct angular range in the slices through the defect region. These results are partially shown in Fig. 7, which gives the circumferential plots for the central defect-region slice and a basal slice. Although not shown, the plots are also quite similar if the angulation is 20° lateral and 40° inferior for both data sets.

Figure 8 shows the limitations of the results when a particular reconstruction is used as the normal and is compared with a reconstruction from a ventricle with a different angulation. Here circumferential plots for the same slice are compared when both data sets do not contain a defect, and when both are angled 40° inferior but one is angled 20° lateral while the other is 40° lateral. The slice shown in the figure is the one that contains the worst discrepancies. The differences indicate the possibility of false positives when looking for defects by comparison of circumferential plots.

For the case of attenuated data, we note without proof that results without attenuation correction are generally less successful in specifically detecting a defect by the difference method than are results with compensation correction.

*Angled left-ventricle phantom.* Figures 9 and 10 show slices through rerotated data for the angled ventricle phantom with and without a defect. In Fig. 9 the slices are parallel to the long axis of the ventricle. The defect can readily be observed and the rest of the shell is mostly unperturbed. These features are shown again in Fig. 10, where the slices are parallel to the short axis of the ventricle; in addition, circumferential plots of the defect slice and an apical slice are shown. The true strength of the

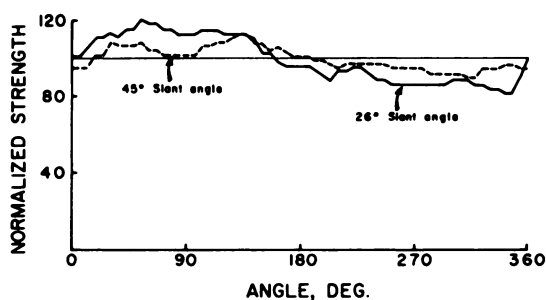


**FIG. 6.** Circumferential plots for slice through rerotated results for half-ellipsoidal shell at level between apex and defect plane. Angulation of long axis is 40° left and 40° inferior. There is no noise, no attenuation, and no attenuation correction. Increasing collimator slant angle improves uniformity toward straight line that is ideal for this slice.

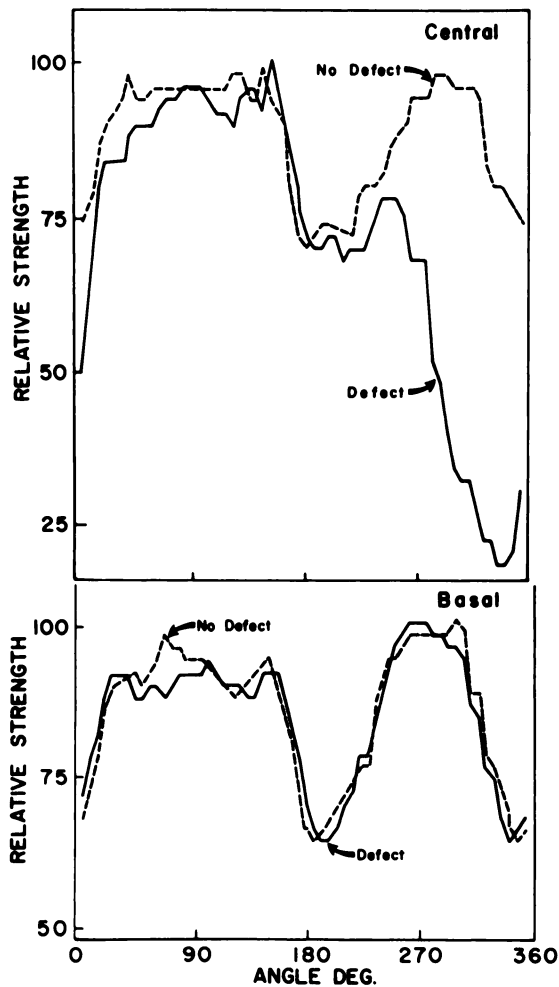


FIG. 7. Circumferential plots for slices through rerotated results for half-ellipsoidal shell. Angulation is as in Fig. 5. Noise and attenuation are included, and attenuation compensation is applied. Between defect and no-defect data sets, there is good agreement in basal slice and there is good dissimilarity over correct angular range (270° to 360°) in central slice that went through defect region.

defect (0%) is seen to be not completely recovered, but the difference between defect and nondefect plots is good. The images shown are with  $T, 1/\sqrt{T}$  attenuation correction, but attenuation compensation produces a similar result. With  $T, 1$  correction, the difference is reduced.

The difference, shown in Fig. 10 with the real data, is smaller than that with the simulated data. This finding is ascribed to Compton scattering.

#### DISCUSSION

When considering two views compared with one view, first of all it is obvious that the two views provide much better geometrical accuracy. Also it is generally held that one-view systems must sacrifice looking for apical defects altogether, whereas the two-view system presented here appears to have the potential for detecting them. Finally, one-view systems have their greatest usefulness when

looking exactly down the long axis of the left ventricle, in which case the symmetry of the object aids in the detection of defects lying in the plane perpendicular to the long axis. This geometrical condition is, however, difficult to obtain in the clinic. The data of this paper do not indicate any such critical condition for two-view tomography.

When considering two-view tomography on its own, we speculated in Ref. 5 that simulation results from perfectly consistent data (i.e., data generated by forward projection of the digitized object rather than by a closed form expression for the length of a ray through a geometric object) would produce perfectly uniform reconstructions without increased polar cap activity. This speculation is not born out by the present results. Moreover, increasing the slant angle to 45°, in which case the Fourier volume is completely covered, does not produce ideal uniformity. We now assign the problem to the nonuniform sampling of the Fourier volume.

For two views of the spherical shell with a defect but without attenuation effects, the results are quite acceptable. However, as the object becomes even less symmetric and with the inclusion of attenuation, nonuniformity becomes bad enough to be called artifact.

The results of attenuation correction are somewhat disappointing. The accuracy measure employed is sensitive to the absolute equivalence of reconstructed strengths compared with the object strengths. Good values for the measure are of interest, but they can occur at the same time that nonuniformities in certain slices are large; this result is the case for the  $T, T$  correction. On the other hand,  $T, 1/\sqrt{T}$  and  $T, 1/T$  corrections produce poorer absolute values but the uniformity in the artifact slice is better. Attenuation compensation is similarly desirable because it produces a strong defect that leads to better distinction between defect and artifact. Nevertheless, with the correction methods tried, it is not possible to get artifact-free results.

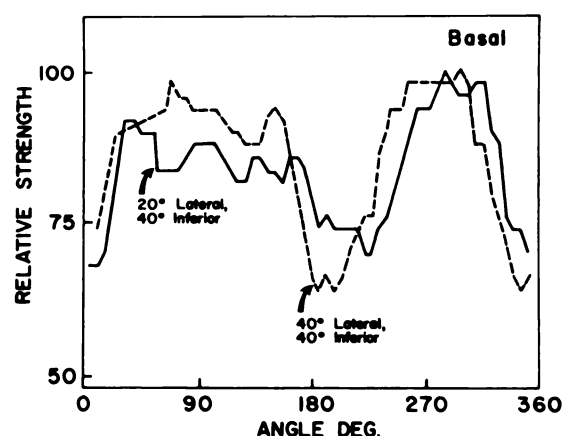
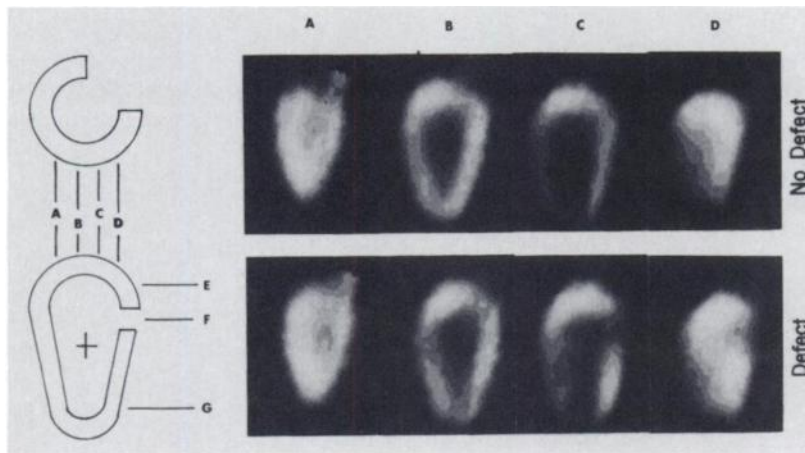


FIG. 8. Worst-case slice difference in circumferential plots for normal (no defect) ellipsoidal shell at two angulations differing by 20°. (Other parameters are as in Fig. 7.)



**FIG. 9.** Reconstructions from two sets of experimental angled left-ventricle-phantom data that differ by addition of a 5-ml defect, as shown in sketch at left. Imaging geometry is as shown in Fig. 4. Reconstruction is with  $T, 1/\sqrt{T}$  attenuation correction. Slices presented in this figure are parallel to long axis, 2.2 mm thick, separated by 1.1 cm, and located as shown. "Horn" artifact in Slice A is atypical of simulation or similar phantom measurements. It is probably due to projection of some of data off edge of camera in lateral view.

However, it is possible to detect a defect by comparison of the circumferential plot results with and without a defect. Therefore, the 2-view technique is probably most appropriate for studies involving stress followed by redistribution on a single patient using thallium. There is also fairly good capability for establishing a set of normal results, since reconstructions are fairly insensitive to the angulation of the ventricle, at least to the extent tested.

**CONCLUSIONS**

For a limited-angular-range collimator, it has been shown that two-view tomography does a much better job of correctly imaging a left-ventricle model as a whole than does one-view tomography. It has also been shown that in imaging defects on which one-view tomography does its best job, the two-view system does not do a

completely satisfactory job when attenuation is included, presumably because of nonuniform sampling. In this case, however, it is possible to detect defects with two views by establishing a normal result and looking for variations from this result. Moreover, two-view reconstructions do not appear to be sensitive to the angulation of the long axis of the ventricle, whereas it is known that one-view reconstructions are. It remains to be shown how severe the effects of attenuation variations and background are in the clinical situation and how insensitive the difference method is to the range of ventricle angulations possible.

**ACKNOWLEDGMENTS**

This investigation was supported by PHS grant number 5 ROI GM 28305-02. In its second year, the grant was reassigned to and awarded by the National Cancer Institute, DHHS, under the number 8 ROI CA 32866-02.

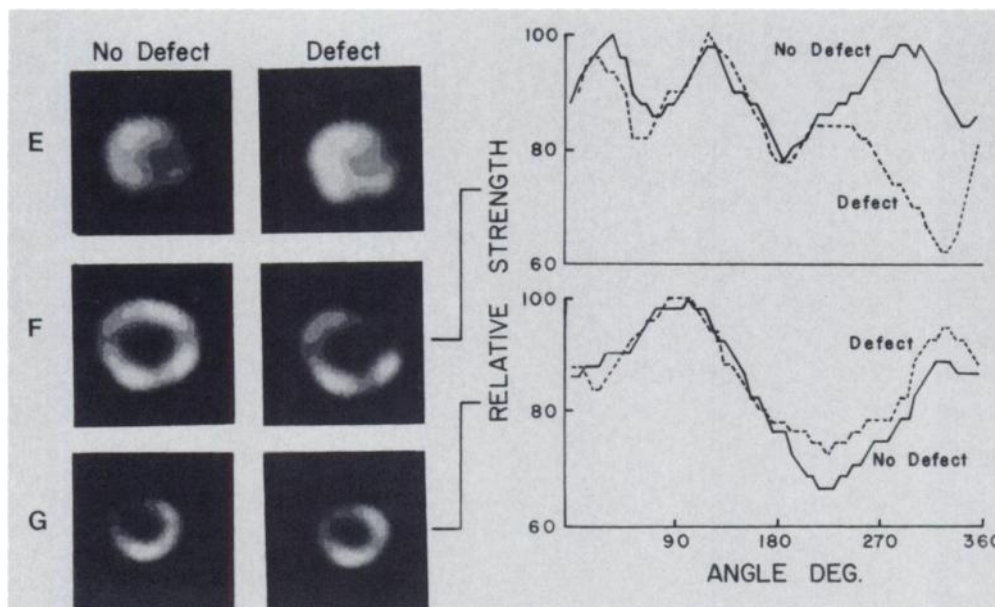


**FIG. 10.** Slices perpendicular to long axis of rerotated results at depths indicated by E, F, and G in Fig. 9. Slices are 6.6 mm thick for nondefect planes and 8.8 mm thick for plane centered on defect. In circumferential plots there is large difference at location of defect in plane F, but only small difference elsewhere.

REFERENCES

1. VOGEL RA, KIRCH D, LEFREE MT, et al: A new method of multiplanar emission tomography using a seven pinhole collimator and an Anger scintillation camera. *J Nucl Med* 19:648-654 1978
2. KORAL KF, ROGERS WL, KNOLL GF: Digital tomographic imaging with a time-modulated pseudorandom coded aperture and Anger camera. *J Nucl Med* 16:402-413, 1975
3. GOTTSCHALK SC, SMITH KA, WAKE RH: Comparison of seven pinhole and rotating slant hole tomography of a cardiac phantom. *J Nucl Med* 21:P27, 1980
4. CHANG W, LIN SL, HENKIN RE: A rotatable quadrant slant hole collimator for tomography (QSH): A stationary scintillation camera based SPECT system. In *Single Photon Emission Computed Tomography and Other Selected Computer Topics*. Sorenson JA, ed. Society of Nuclear Medicine, New York, 1980, p 81
5. TAM KC, PEREZ-MENDEZ V, MACDONALD B: 3-D object reconstruction in emission and transmission tomography with limited angular input. *IEEE Trans Nucl Sci* NS-26:2797-2805, 1979
6. LENT A, TUY H: An iterative method for the extrapolation of band-limited functions. State University of New York at Buffalo, Department of Computer Science, Technical Report No. MIPG 35, 1979
7. BIZAIS Y, ZUBAL IG, ROWE RW, et al: Potentiality of D7PHT for dynamic tomography. *J Nucl Med* 24:P75, 1983
8. KORAL KF, CLINTHORNE NH, ROGERS WL, et al: Feasibility of sharpening limited-angle tomography by including an orthogonal set of projections. *Nucl Instrum Meth* 193: 223-227, 1982
9. COFFEY JL, CRISTY M, WARNER GG: Specific absorbed fractions for photon sources uniformly distributed in the heart chambers and heart wall of a heterogeneous phantom. *J Nucl Med* 22:65-71, 1981
10. CHANG W, HENKIN RE: Performance of the rotating slant-hole collimator for the detection of myocardial perfusion abnormalities. *J Nucl Med* 23:547, 1982
11. LEFREE MT, VOGEL RA, KIRCH DL, et al: Seven-pinhole tomography—A technical description. *J Nucl Med* 22:48-54, 1982
12. JASZCZAK RJ, CHANG L-T, STEIN NA, et al: Whole-body single-photon emission computed tomography using dual, large-field-of-view scintillation cameras. *Phys Med Bio* 24: 1123-1143, 1979
13. BORRELLO JA, CLINTHORNE NH, ROGERS WL, et al: Oblique-angle tomography: A restructuring algorithm for transaxial tomographic data. *J Nucl Med* 22:471-473, 1981